REPORT DOCUMENTATION PAGE

AFRL-SR-BL-TR-00-

0579

1. AGENCY USE ONLY *(Leave blank)*	2. REPORT DATE	3.
	3 October 2000	Final Technical Report - 1 May 199 TO 1 July 2000

4. TITLE AND SUBTITLE
DESIGN AND THERMO-MECHANICAL CHARACTERIZATION OF NiTi SMART COMPOSITES.

5. FUNDING NUMBERS
F49620-99-1-0245

6. AUTHOR(S)
Dr. John Shaw

7. PERFORMING ORGANIZATION NAME(S) AND ADDRESS(ES)
University Of Michigan
College Of Engineering
1320 Beal Ave.
Ann Arbor, Michigan 48109-2140

8. PERFORMING ORGANIZATION REPORT NUMBER

9. SPONSORING/MONITORING AGENCY NAME(S) AND ADDRESS(ES)
AFOSR/NA
801 N. Randolph St., Rm 947
Arlington, VA 22203

10. SPONSORING/MONITORING AGENCY REPORT NUMBER

11. SUPPLEMENTARY NOTES

12a. DISTRIBUTION AVAILABILITY STATEMENT
Approved for public release; distribution is unlimited

12b. DISTRIBUTION CODE

13. ABSTRACT *(Maximum 200 words)*

This report describes research performed over 15 months to investigate the issues associated with the design and characterization of composite elements with embedded shape memory alloy (SMA) elements. The ultimate objective was to design structural elements that have adaptive capabilities. This exploratory effort addressed the choice of constituent materials and their characterization, certain manufacturing issues, and transformation fronts in an SMA fiber. It also assessed a simple approach based on a shear-lag analysis to determine critical geometric parameters for the design of unidirectional SMA fiber/elastic matrix active composites

20001023 048

14. SUBJECT TERMS
DESIGN AND THERMO-MECHANICAL CHARACTERIZATION OF NiTi SMART COMPOSITES.

15. NUMBER OF PAGES

16. PRICE CODE

17. SECURITY CLASSIFICATION OF REPORT	18. SECURITY CLASSIFICATION OF THIS PAGE	19. SECURITY CLASSIFICATION OF ABSTRACT	20. LIMITATION OF ABSTRACT
Unclassified	Unclassified	Unclassified	UL

Final Technical Report

Design and Thermo–Mechanical Characterization of NiTi Smart Composites[1]

John A. Shaw[2] and Bichiau Chang[3]

Department of Aerospace Engineering
The University of Michigan

October 3, 2000

[1]AFOSR Grant: F49620-99-1-0245, May 1999 to July 2000, AFOSR Scientific Officers: Dr. H. Thomas Hahn and Dr. Walter F. Jones

[2]Assistant Professor (Director, Adaptive Materials and Structures Lab), 1320 Beal Ave, Ann Arbor, MI 48109-2140, (734) 764-3395, (734) 763-0578 (fax), jashaw@engin.umich.edu

[3]Graduate student

Abstract

This report describes research performed over 15 months to investigate the issues associated with the design and characterization of composite elements with embedded shape memory alloy (SMA) elements. The ultimate objective was to design structural elements that have adaptive capabilities. This exploratory effort addressed the choice of constituent materials and their characterization, certain manufacturing issues, and transformation fronts in an SMA fiber. It also assessed a simple approach based on a shear–lag analysis to determine critical geometric parameters for the design of unidirectional SMA fiber/elastic matrix active composites.

Nomenclature

Variable	Description
x	axial position
r	radial position
R	specimen radius
a	fiber radius
L	specimen half–length
σ_m	matrix axial stress
τ_m	matrix shear stress
τ_I	interface shear stress
σ_f	fiber axial stress
u_f	fiber axial displacement field
u_m	matrix axial displacement field
γ_m	matrix shear strain
ϵ_f	fiber axial strain
$\bar{\epsilon}_m$	far field matrix axial strain
ϵ_0	fiber pre–strain
β	fiber transformation strain
G_m	matrix shear modulus
E_f	fiber elastic modulus
E_A	austenite elastic modulus
E_M	martensite elastic modulus
ξ	detwinned martensite phase fraction

1 Introduction

Shape Memory Alloys (SMAs), such as NiTi (or Nitinol), exhibit two remarkable properties, the shape memory effect and pseudoelasticity (see Fig. 1). The shape memory effect is the material's ability to erase large mechanically-induced strains (up to 8%) by moderate increases in temperature (≈10–20 °C). Pseudoelasticity refers to the ability of the material in a somewhat higher temperature regime to accommodate strains of this magnitude during loading and then recover upon unloading (via a hysteresis loop). The underlying mechanism is a reversible martensitic transformation between solid-state phases, often occurring near room temperature. The transformation can be induced by changes in temperature or by changes in stress due to the strong thermo-mechanical coupling in the material behavior. The material also has very nonlinear mechanical behavior, high internal damping, and high yield stresses. All of these properties make NiTi a promising candidate for novel structural applications (see *Perkins (Ed.)* (1975), *Funakubo (Ed.)* (1987), *Duerig et al.* (1990) and *Otsuka and Wayman (Ed.)* (1998)).

The extreme sensitivities to temperature and stress of NiTi-based SMAs can be exploited to produce large mechanical deformations and/or stresses. Due to its much larger work output capability and control authority over other so-called smart materials, NiTi is advantageous for applications that require only moderate response times (more than 1 sec). When embedded in a conventional material, NiTi can be used in a passive role to improve the structural integrity (stiffness, ductility, damping, energy absorption, etc.) by exploiting its large strain recovery mechanism, high yield strength, and high damping capacity. In an active role, the thermal sensing and actuation capability of NiTi can be used. Since the transformation temperatures can be tailored by the material processing, pre-tensioned NiTi fibers could be used in principle to twist and bend thin beam and shell composite structures. Such composites would have potential use for adaptive airfoils in advanced air

vehicles. The temperature sensing capability could be used, for example, to cause large deformations suitable for deicing along the leading edge of an aircraft wing or helicopter rotor blade. Such composites could also act as active frequency tuning elements, leading to improvements in vibration and flutter control of airfoils. These would avoid the use of moving parts and may facilitate more compact, lighter weight designs.

NiTi's remarkable behavior arises from the interplay of two phases, a high temperature phase (austenite), having a cubic lattice structure, and a low temperature phase (martensite), having a monoclinic structure (*Otsuka et al.*, 1971). Due to its low degree of symmetry, the martensite phase exists either as a randomly twinned structure (low temperature, low stress state) or a stress-induced detwinned structure that can accommodate relatively large, reversible strains. The last decade has seen some significant experimental findings regarding the thermo–mechanical behavior of SMAs (see *Leo et al.* (1993), *Shaw and Kyriakides* (1995), *Sittner et al.* (1995), and *Gall et al.* (1999)), providing new impetus for design and application. In particular, few of the SMA constitutive models acknowledge the material instabilities which have been observed in pseudoelastic NiTi (*Shaw and Kyriakides*, 1997). For notable exceptions see *James* (1983), *Abeyaratne and Knowles* (1993), and *Knowles* (1999), and *Shaw* (2000).

The behavior of NiTi is quite complex and limited experimental work has yet been done to understand the behavior of NiTi integrated composites. The issues are formidable – complex manufacturing process, anisotropic behavior, strong thermal–mechanical coupling, matrix–fiber compatibility, complex failure mechanisms, and material instabilities. Initial attempts by *Liang et al.* (1989) to embed NiTi wires into a polymer matrix proved somewhat unsuccessful due to manufacturing difficulties and poor interfacial bonding. *Baz and Ro* (1992) included rubber sleeves between the SMA wires and the composite laminate to minimize the strain mismatch. *Hebda et al.* (1995) used a graphite/epoxy composite with embedded two–way shape memory NiTi wires, leading to a simpler fabrication procedure. *Johnalagadda et al.* (1997) conducted experiments to compare the interfacial bond strength between the epoxy matrix and SMA wires processed by various surface treatment, including acid etched, hand sanded, and sandblasted. *de Blonk and Lagoudas* (1998) used elastomeric rods with embedded two–way shape memory NiTi wires.

2 Critical Issues

The problem of designing an active SMA composite (compared to a passive SMA composite) is especially difficult and is the focus of this report. It will be assumed here that the objective is to design an active SMA composite that produces a predefined shape change, say a simple bending element that takes different curvature values for some hot and cold values of temperature. One is faced with the following issues:

- *Compatibility between matrix and SMA material.* Several attempts have been made to embed prestretched SMA wires in an epoxy/carbon–fiber composite. In most cases the composite actuates upon heating but then does not return during the cooling part of the actuation cycle. This is likely due to the strain mismatch between the matrix material and the 5 to 8% strain recovery in the SMA wire. The matrix either yields plastically or else debonds along the interface. This makes ceramics, metals, and most polymers (including conventional graphite fiber/epoxy matrix composites) poor choices for matrix materials of such active composites.

  To overcome these difficulties we chose an elastomer material (DOW Silicone RTV rubber Silastic T-2) for the matrix. The material vulcanizes at room temperature and is optically transparent when cured. Adhesion between the SMA fiber and the

elastomer may still be an issue, but the matrix can clearly withstand the changes in fiber strain without yielding.

- *Topology of SMA elements within the matrix.* Many different topologies can be envisioned. Here, SMA wires were chosen since this form generally produces the largest transformation strains. It is also the most common and least expensive form. For simplicity we first attempted a uni–directional fiber composite.

- *SMA transition temperature and composite manufacturing.* Commercial grade NiTiCu SMA wire (K-alloy from Memry Corp.) was obtained with an austenite start temperature of 50 to 60 °C, depending on heat treatment (see Fig. 4). This ensured that the SMA wires remained in a martensitic state during the room temperature composite cure. One (or more) SMA Wire was prestrained at room temperature, placed into a mold (a glass tube in this case), and then the elastomer was poured and cured. After mixing the curing agent with the rubber base the mixture usually contained a significant quantity of bubbles which led to voids after curing. The bubbles were removed by rotating a glass tube of the mixture at high speed (approx. 1000 rpm). This created a void along the rotation axis. Any bubbles present were forced to the axis of rotation due to the centrifugal effects and then percolated out of the material into the center void (see Fig. 2). Once the mixture was cured (36 hours), the mold was cut away leaving a silicone rubber rod with a prestrained, embedded SMA wire. (Another method that could improve the performance of the composite by optimizing the strain change during heating would have been to maintain the SMA wire under tension during curing, but this was not done for ease of manufacture.)

- *Biasing of SMA elements during cooling.* The shape memory effect during heating will result in recovery of strain only if a prestrain is imposed during the cooling portion of a temperature cycle. Therefore, a biasing mechanism was needed to return the SMA to its high strain state during cooling. In devices this is often accomplished with mechanical springs of an intermediate stiffness between that of the martensite and austenite. Here, we used the stored elastic energy in the matrix material (after heating of the composite) to reset the SMA wire to its high strain state upon cooling. This required a careful design of the geometric and material parameters of the composite to achieve reliable cyclic operation.

  Another approach that could have been use was to induce a two–way shape memory effect in the SMA wire, whereby the wire would shorten upon heating and spontaneously elongate during cooling. This has been tried by a few investigators (see, for example, *de Blonk and Lagoudas* (1998)). We elected not to use this approach, since the strain changes are smaller (only 0.5 to 1%) than for the one–way shape memory effect, and we were concerned about the reduced fatigue performance of the SMA resulting from the severe thermo–mechanical processing needed to induce the two–way effect.

As described above a 0.42 in diameter, 6.25" long RTV silicon rubber rod was manufactured with a 0.022 in NiTi wire. The NiTi wire was installed with a stress–free 5% prestrain (see Fig. 5) off–axis by approximately 0.07 in (see Fig. 6). The rod was then immersed in a 70 °C bath of water. The rod bent as expected when hot (approx. 1" deflection), but did not return to a straight configuration upon cooling back to room temperature (approx. 1/4" deflection). This was expected, since the martensitic state is quite hysteretic. However, after a single thermal cycle little curvature change was observed thereafter. Because the rubber was transparent, it was noticed that the wire had debonded from the rubber matrix near the ends. To improve the adhesion between the SMA wire and the rubber

matrix another specimen was made in which the SMA wire was first coated with a rubber adhesive (DOW RTV sealant 832). This improved the adhesion, and seemed to produce repeatable curvature changes from the hot and cold configurations (see Fig. 7). However, it was not clear whether the geometry of our prototype was optimal and analytical design tools were needed to guide our further prototype development.

Another experiment was conducted on flat dog–bone specimens with on–axis, pre-strained SMA wires (see Fig. 8). These were manufactured by filling a mold (see Fig. 9) halfway, allowing it to partially cure, placing three SMA wires atop longitudinally, filling the remainder of the mold, and allowing the specimen to cure completely. In Figure 10 the tabs were cut off a specimen, leaving a rectangular plate, and images were taken of the cantilevered specimen as it cooled down from over 70 °C. A small 0.003 in K–type thermocouple was inserted into the backside of the beam against one of the SMA wires to monitor the temperature. The beam was loaded only by it own weight, and it sagged noticeably as the SMA wire transformed from austenite to martensite during cooling.

3 Design Approach

Despite the fact that the experiments discussed above involved primarily bending deformations, we chose to focus on the simplified problem of uniaxial self–stressing during thermal cycling. We hoped this would shed some light on the elastic interactions between the SMA element and the surrounding matrix material. For an active composite, two competing criteria for the relative stiffness of the matrix vs. SMA material emerged from our experience with the prototype specimens. First, the matrix material must be stiff enough to generate large axial stresses upon heating the SMA wire to its austenite state. These stresses are necessary to generate sufficient axial stress in the SMA fiber to produce detwinned martensite (large strain) upon cooling. Second, the matrix material must not be so stiff as to cause permanent yielding of the SMA fiber or debonding at the SMA/matrix shear interface. Given the chosen material systems, we had two geometric design parameters at our disposal, the ratio of SMA wire to specimen diameter (or volume fraction of SMA material) and the aspect ratio of the SMA wire (or length to diameter ratio). We set out to optimize these two parameters for given desired fiber stress and maximum interfacial shear stress.

3.1 Shear–lag Analysis Derivation

The simplest analytical approach that could guide our future designs is a slightly modified version of the classical shear–lag analysis of *Cox* (1952). The shear–lag analysis has been used extensively to study the shear stress transfer between fiber and matrix constituents in conventional composite structures. We are aware, of course, of the limitations of the shear–lag approach; notwithstanding its popularity, it is clearly an approximate method that should be used with care. *Nairn* (1997), in particular, has challenged the validity of the Cox shear–lag analysis and has derived a similar second order differential equation for the fiber axial stress, but with a different coefficient. A comparison will be made between the two approaches.

A derivation of our modified shear–lag analysis is given here for clarity. Unlike conventional fibers, uniaxially loaded SMA wires can develop transformation fronts with steep strain gradients of phase separating uniform phases. Such transformation fronts have been studied extensively in *Shaw and Kyriakides* (1995) and *Shaw and Kyriakides* (1997). To our knowledge this possibility has never been studied in the context of a shear–lag analysis. In addition, our focus is on the residual stress fields generated during temperature changes, rather than those due to external loading.

We consider a model problem of an SMA fiber embedded along the axis of a cylindrical linear elastic matrix (see Fig. 11). Small strain kinematics are assumed, consistent with the expected strains of a few percent. We treat state (a) in Fig. 11 as the reference configuration of the SMA wire, since stress–free austenite is a unique state and it simplifies the constitutive description. State (d) in Fig. 11, which is also stress–free, is treated as the reference configuration for the matrix material. Consequently, the kinematic condition for perfect bonding between the pre–strained fiber and matrix is

$$u_f(x) = u_m(x, a) + \epsilon_0 x, \tag{1}$$

where u_f and u_m are the displacement fields of the fiber and matrix, respectively, and ϵ_0 is the prestrain in the fiber. Equilibrium of the matrix annulus of Fig. 12 in axial direction neglecting $\frac{\partial \sigma_m}{\partial x}$ is

$$\tau_m(x, r) = \tau_I(x)\frac{a}{r}. \tag{2}$$

The matrix shear response is approximated as

$$\tau_m = G_m \gamma_m \approx G_m \frac{\partial u_m}{\partial r}. \tag{3}$$

by neglecting the part of the shear strain $\frac{\partial v_m}{\partial x}$. Combining equations (2) and (3) gives

$$\frac{\partial u_m}{\partial r}(x, r) = \frac{r}{a}\frac{\tau_I(x)}{G_m}. \tag{4}$$

Now, integrating eq. (4) in the radial direction gives

$$u_m(x, r) - u_m(x, a) = a\frac{\tau_I(x)}{G_m}\ln\left(\frac{r}{a}\right). \tag{5}$$

Evaluating the far field displacement $\tilde{u}_m(x) \equiv u_m(x, R)$ and including the compatibility condition (eq. 1) at the interface produces

$$\tilde{u}_m(x) = u_f(x) - \epsilon_0 x + a\frac{\tau_I(x)}{G_m}\ln\left(\frac{R}{a}\right). \tag{6}$$

Equilibrium of the fiber in the axial direction (see Fig. 13) is

$$\frac{d\sigma_f}{dx} = -2\frac{\tau_I(x)}{a}. \tag{7}$$

Substituting for τ_I gives

$$\frac{d\sigma_f}{dx} = -2\frac{G_m}{a^2}\left[\frac{\tilde{u}_m(x) - u_f(x) + \epsilon_0 x}{\ln(R/a)}\right]. \tag{8}$$

The idealized SMA fiber uniaxial constitutive relation (see Fig. 14) is

$$\sigma_f = E_f(\xi)\left[\epsilon_f - \beta\xi\right]. \tag{9}$$

where ξ is the fraction of detwinned martensite, β is the stress–free transformation strain, and the fiber modulus is

$$E_f(\xi) = E_A + \xi(E_M - E_A). \tag{10}$$

Differentiating eq. (8) with respect to x and substituting eq. (9) gives

$$\frac{d^2\sigma_f}{dx^2} - \lambda^2\sigma_f = -\lambda^2 E_f(\xi)\left[\tilde{\epsilon}_m - \beta(\xi - \xi_0)\right]. \tag{11}$$

where ξ_0 is the initial martensite fraction caused during prestraining, $\tilde{\epsilon}_m$ is the far field matrix axial strain, and the Cox parameter is defined as

$$\lambda^2 \equiv \frac{1}{a^2} \frac{2G_m}{E_f \ln(R/a)}. \tag{12}$$

Assuming the SMA fiber is stress–free at its ends gives the boundary conditions

$$\sigma_f(L) = \sigma_f(-L) = 0, \tag{13}$$

and due to symmetry at the midplane

$$\frac{d\sigma_f(0)}{dx} = 0. \tag{14}$$

In general $\xi(x)$ will be a nonuniform field quantity. During the heat up phase, we expect that transformation fronts will propagate from the ends towards the midplane of the specimen. This is idealized as a step function (for the symmetric half $0 < x < L$) as

$$\xi(x) = \begin{cases} \xi_0 & : \quad 0 < x < s \\ 0 & : \quad s < x < L \end{cases} \tag{15}$$

where s is the position of a transformation front separating martensite and austenite phases. During the transformation, the matching conditions at $x = s$ are

$$\begin{aligned} [[\sigma_f(s)]] &= 0 \\ \left[\left[\frac{d\sigma_f(s)}{dx}\right]\right] &= 0 \end{aligned} \tag{16}$$

where [[.]] refers to the jump in the quantity. The second part of eq. 16 is a consequence of the continuity of the right hand side of eq. 8.

It will be convenient to introduce non–dimensional axial positions, $\overline{x} \equiv x/L$ and $\overline{s} \equiv s/L$. Non-dimensional fiber and interface stresses are defined as

$$\begin{aligned} \overline{\sigma} &\equiv \sigma_f/E_f \\ \overline{\tau_I} &\equiv \tau_I/G_m. \end{aligned} \tag{17}$$

This leave three relevant parameters, two geometric ratios and two material property ratios.

$$\begin{aligned} \overline{a} &\equiv a/R \\ \overline{L} &\equiv L/R \\ \overline{G} &\equiv G_m/E_A \\ \overline{E}_M &\equiv E_M/E_A \end{aligned} \tag{18}$$

From these a non–dimensional Cox parameter can be defined.

$$\overline{\lambda} \equiv \frac{\overline{L}}{\overline{a}} \sqrt{\frac{2\overline{G}}{\ln(1/\overline{a})}} \tag{19}$$

Now the governing second–order differential equation becomes

$$\frac{d^2\overline{\sigma}}{d\overline{x}^2} - \overline{\lambda}^2 \overline{\sigma} = -\overline{\lambda}^2 \left[\tilde{\epsilon}_m - \beta(\xi - \xi_0)\right]. \tag{20}$$

with boundary conditions

$$\begin{aligned} \frac{d\bar{\sigma}(0)}{d\bar{x}} &= 0 \\ \bar{\sigma}(1) &= 0 \end{aligned} \tag{21}$$

and matching conditions

$$\begin{aligned} [[\bar{\sigma}(\bar{s})]] &= 0 \\ \left[\left[\frac{d\bar{\sigma}(\bar{s})}{d\bar{x}}\right]\right] &= 0 \end{aligned} \tag{22}$$

From here on the "bars" will be dropped from the notation and all quantities will be understood to be non-dimensional.

$$\begin{aligned} \frac{d^2\sigma_f}{dx^2} - \lambda^2\sigma_f &= -\lambda^2\left[\bar{\epsilon}_m - \beta(\xi - \xi_0)\right]. \\ \frac{d\sigma_f(0)}{dx} &= 0 \\ \sigma_f(1) &= 0 \\ [[\sigma_f(s)]] &= 0 \\ \left[\left[\frac{d\sigma_f(s)}{dx}\right]\right] &= 0 \end{aligned} \tag{23}$$

3.2 Analytical Results

Here we consider the solution to the shear lag problem in two parts, first the complete transformation then the evolution of partial transformations.

3.2.1 Complete transformation

When the composite is sufficiently heated past the austenite finish temperature the SMA fiber transforms to austenite and recovers most of the prestrain. The phase fraction of martensite is zero everywhere ($\xi = 0$). The non–dimensional stress in the fiber with no external loading ($\bar{\epsilon}_m = 0$, zero far–field strain) is

$$\sigma_f(x) = \beta\xi_0\left[1 - \frac{\cosh(\lambda x)}{\cosh(\lambda)}\right], \tag{24}$$

and the non–dimensional interfacial shear stress is

$$\tau_I(x) = \frac{\beta\xi_0\lambda}{2G}\frac{a}{L}\frac{\sinh(\lambda x)}{\cosh(\lambda)}. \tag{25}$$

The fiber stress has a maximum at the midplane $x = 0$; whereas, the magnitude of the interfacial shear stress is maximum at the edges $x = \pm 1$.

$$\sigma_{f_{max}} = \sigma_f(0) = \beta\xi_0\left[1 - \frac{1}{\cosh(\lambda)}\right] \tag{26}$$

$$\tau_{I_{max}} = \tau_I(1) = \frac{\beta\xi_0\lambda a}{2G}\tanh(\lambda). \tag{27}$$

Typical values for transformation strain, $\beta = 0.05$, and initial fraction of martensite, $\xi_0 = 1$, (or a fiber prestrain $\epsilon_0 = 0.05$) are assumed from here on. The austenite elastic modulus is $E_A = 70$ GPa. The matrix (initial) elastic modulus is approximately 3 MPa, giving an isotropic shear modulus of 1 MPa. Therefore, the ratio of matrix shear modulus to fiber modulus is approximately $G = 1/70,000$.

3.2.2 Partial transformation

As the material transforms from martensite to austenite during heating transformation fronts will likely be present. Fronts will move from the ends towards the middle provided the axial stress at the front location remains below the stress in the remaining untransformed length. In this case the jump conditions of eq. (23) must be included and the fiber stress is expressed piecewise as

$$\sigma_f(x) = \begin{cases} \beta \text{sech}\lambda \left[\cosh(\lambda - \lambda s) - 1\right] \cosh \lambda x & : \quad 0 < x < s, \\ \beta \left[\xi_0 - (\text{sech}\lambda + \tanh \lambda \sinh \lambda s) \cosh \lambda x + \sinh \lambda \sinh \lambda x\right] & : \quad s < x < 1 \end{cases} \tag{28}$$

Likewise, the interfacial shear stress is then

$$\tau_I(x) = \begin{cases} \frac{a}{2G} \beta \lambda \text{sech}\lambda \left[1 - \cosh(\lambda - \lambda s)\right] \sinh \lambda x & : \quad 0 < x < s \\ \frac{a}{2G} \beta \lambda \left[(\text{sech}\lambda + \tanh \lambda \sinh \lambda s) \sinh \lambda x - \sinh \lambda \cosh \lambda x\right] & : \quad s < x < 1 \end{cases} \tag{29}$$

The evolution of the fiber stress and the interfacial shear stress are shown in Fig. 16 for some chosen values of a, R, and G. A kink exists in the stress fields due to the presence of fronts. As can be seen in Fig. 16a during front propagation, the maximum fiber stress is not at $x = 0$, but is at $x = s$. The maximum shear stress is still predicted to be at $x = 1$ as seen in Fig. 16b, but the shear stress changes sign near $x = s$. Note, also that unlike typical composites where a clear hyperbolic (or exponential) character is observed, in this case the final axial fiber stress is nearly quadratic and the interfacial shear stress is nearly linear. This means that the chosen fiber length is relatively short compared to the shear–lag boundary layer length. It is also caused by the fact that the ratio of fiber modulus to matrix modulus (G) is nearly five orders of magnitude. The maximum interfacial shear stress is predicted to be quite large, probably unrealistically so. Fig. 17 shows the predicted axial displacement field in the matrix after complete transformation to austenite.

Fig. 18 shows how the non–dimensional midplane stress $\sigma(0)$ varies as a function of the non–dimensional Cox parameter λ. As λ gets larger the stress $\sigma(0)$ gets larger, but eventually reaches an asymptotic value that represents the extreme case of the matrix acting nearly rigid. Fig. 19, in turn, shows how the Cox parameter varies with geometric parameters. The Cox parameter increases dramatically for long, thin wires (large L and small a). (Although not shown, the Cox parameter rises again as a approaches unity, but the assumption of a zero far–field strain is not realistic in this case.)

The dependence of the maximum interfacial shear stress on geometric parameters is shown in Fig. 20. Similar trends exist, i.e., larger stress for long, thin wires, except for very thin wires.

For two given materials there are two geometric parameters available to optimize the design. In general, one desires a high maximum axial stress, but a low interfacial shear stress. Fig. 21 shows the case of a maximum axial stress of 0.0025 E_A and a maximum shear stress of 2 G_m. The predicted optimum design is $a = 0.119$ and $L = 10.5$.

Discussion

Some questions remain whether the Cox shear–lag approach is appropriate for the materials considered here. The unrealistically large interfacial shear stresses predicted by this approach, in particular, raises some doubts. One issue may be that the ratio of the moduli is quite large, several orders of magnitude larger than usually found in conventional composites. In addition, the work of *Nairn* (1997) raises further doubts on the validity of the Cox approach. *Nairn* (1997) derived an alternate shear–lag parameter based on certain

assumptions from linear elasticity theory.

$$\lambda_{Nairn} = \frac{L}{a}\sqrt{\frac{2[a^2 + E_m(1-a^2)]}{\frac{1}{2}(1-a^2)E_m(1+\nu_{wire}) + (1+\nu_m)(\frac{a^2}{2} - \frac{3}{2} - \frac{\ln a^2}{1+a^2})}} \tag{30}$$

Based on comparison with finite element analyses, Nairn considered that his alternate shear–lag approach provides a reasonable approximation for the axial stress distribution, but still provides a poor approximation of the interfacial shear stress.

The dependence of the Nairn parameter on geometric parameters for our materials is shown in Fig. 23. Interestingly, except for very thin wires, λ_{Nairn} increases with increasing wire diameter, a trend which is opposite to that of Cox. Notice also that the values of the Nairn parameter are much larger. A direct comparison of the two parameters is shown in Fig. 24. Note that the ratio of the two parameters becomes alarmingly large as the ratio of the two material moduli becomes large.

Fig. 25 shows the predicted stress distributions using the Nairn parameter. The magnitude and distributions are quite different from that predicted using the Cox parameter. In fact, the assumed front kinetics are no longer valid, since the axial stress at the mid-plane no longer remains a maximum at each instant. Although not shown, if the analysis is to be believed we expect that austenite will nucleate in the center after the initial fronts move a short distance inward from the ends. This will initiate two more fronts, and several more nucleations could in fact be repeated before the transformation is complete.

Further study is clearly necessary to understand the discrepancy between the two approaches. In any event the shear–lag analysis does not seem to provide a plausible design approach for the materials considered here. It neglects radial stresses, which may be important for the debonding problem at the wire/matrix interface. It also assumes small strain kinematics, which is likely not appropriate for the rubbery matrix material. A nonlinear elasticity analysis is probably necessary to develop a design procedure with confidence.

Conclusions

The objective in the proposed work was to develop successful NiTi/elastomer composites that have adaptive capabilities and to develop effective design tools. The potential benefits to Air Force applications are in the development of new materials, thereby leading to weight savings, improved damage tolerance, vibration suppression, and the active control of aerospace structures.

Manufacturing techniques were developed for active composite elements using silicone rubber and prestrained, shape memory alloy wires. Progress was made in solving some of the strain mismatch problems that have plagued other previous attempts. Interesting active and passive features were demonstrated experimentally as the ambient temperature was changed.

A design methodology was developed based on a classical shear lag approach. The analytical results were less satisfactory than the experimental results, predicting excessively large interfacial shear stresses. In addition, the use of the classical shear lag parameter by Cox and an improved one by Nairn give contradictory trends, leading to further doubts about the validity of the shear–lag approach. The issue seems to be exacerbated by the extremely large ratio of elastic moduli for the materials used here. In the future, we recommend that the shear–lag approach be abandoned for this material system. A full three–dimensional solution, using finite elements, is probably necessary to achieve confidence in the analytical predictions. This will require nonlinear finite deformation elasticity for the matrix material and an accurate one–dimensional model for the SMA elements. Efforts in this direction are ongoing.

Acknowledgement

The financial support of the U.S. Air Force Office of Scientific Research is greatly appreciated. The grant provided partial support of a doctoral student, one summer month salary for the PI, and some laboratory supplies for conducting experiments in the Adaptive Materials and Structures Laboratory at the University of Michigan.

References

R. Abeyaratne and J. K. Knowles. A continuum model of a thermoelastic solid capable of undergoing phase transitions. *Journal of the Mechanics and Physics of Solids*, 41:541–571, 1993.

A. Baz and J. Ro. Thermo–dynamic characteristics of Nitinol reinforced composite beams. *Composites Engineering*, 2:527–542, 1992.

H. L. Cox. Stresses on and around fibres in a composite. *British Journal of Applied Physics*, 3:72–79, 1952.

B. J. de Blonk and D. C. Lagoudas. Actuation of elastomeric rods with embedded two–way shape memory alloy actuators. *Smart Materials and Structures*, 7:771–783, 1998.

T. W. Duerig, K. N. Melton, D. Stöckel, and C. M. Wayman (Ed.). *Engineering Aspects of Shape Memory Alloys*. Butterworth-Heinemann, 1990.

H. Funakubo (Ed.). *Shape Memory Alloys*. Gordon and Breach Science Publishers, 1987.

K. Gall, H. Sehitoglu, Y. Chumlyakov, and I. Kireeva. Tension-compression asymmetry of the stress-strain response in aged single crystal and polycrystalline NiTi. *Acta Materialia*, 47(4):1203–1217, 1999.

D. A. Hebda, M. E. Whitlock, J. B. Ditman, and S. R. White. Manufacturing of adaptive graphite/epoxy structures with embedded Nitinol wires. *Journal of Intelligent Materials and Smart Systems*, 6(2):220–228, 1995.

R. D. James. Displacive phase transformations in solids. *Journal of the Mechanics and Physics of Solids*, 34(4):359–394, 1983.

K. Johnalagadda, G. E. Kline, and N. R. Sottos. Local displacement and load transfer in shape memory alloy composites. *Experimental Mechanics*, 37(1):78–86, 1997.

J. K. Knowles. Stress-induced phase transitions in elastic solids. *Computational Mechanics*, 22:429–436, 1999.

P. H. Leo, T. W. Shield, and O. P. Bruno. Transient heat transfer effects on the pseudoelastic behavior of shape-memory wires. *Acta Metallurgica et Materialia*, 41:2477–2485, 1993.

C. Liang, J. Jia, and C. Rogers. Behavior of shape memory alloy reinforced composite plates part ii. *Proceedings of the 30th Structures, Structural Dynamics and Materials Conference, Mobile, AL, AIAA-89-1331-CP*, pages 1504–1513, 1989.

J. A. Nairn. On the use of shear–lag methods for analysis of stress transfer in unidirectional composites. *Mechanics of Materials*, 26:63–80, 1997.

K. Otsuka and C. M. Wayman (Ed.). *Shape Memory Materials*. Cambridge University Press, 1998.

K. Otsuka, T. Sawamura, and K. Shimizu. Crystal structure and internal defects of equiatomic TiNi martensite. *Phys. State. Sol. (A)*, 5:457, 1971.

J. Perkins (Ed.). *Shape Memory Effects in Alloys*. Plenum Press, 1975.

J. A. Shaw and S. Kyriakides. Thermomechanical aspects of NiTi. *Journal of the Mechanics and Physics of Solids*, 43(8):1243–1281, 1995.

J. A. Shaw and S. Kyriakides. On the nucleation and propagation of phase transformation fronts in a NiTi alloy. *Acta Materialia*, 45(2):673–700, 1997.

J. A. Shaw. Thermo-mechanical simulations of localized thermo–mechanical behavior in a NiTi shape memory alloy. *International Journal of Plasticity*, 46(5):541–562, 2000.

P. Sittner, M. Takakura, and M. Tokuda. The stabilization of transformation pathway in stress induced martensite. *Scripta Metallurgica et Materialia*, 32(12):2073–2079, 1995.

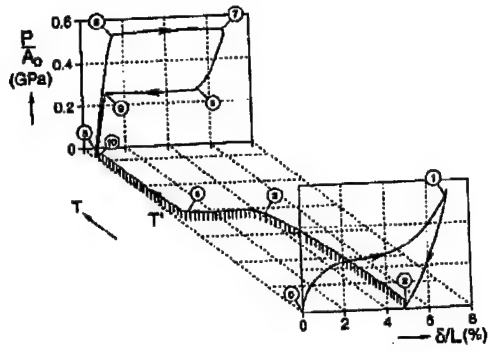

Figure 1: Thermo-mechanical response of NiTi wire in water: shape memory effect ⓪ → ④; pseudoelastic response ⑤ → ⑩.

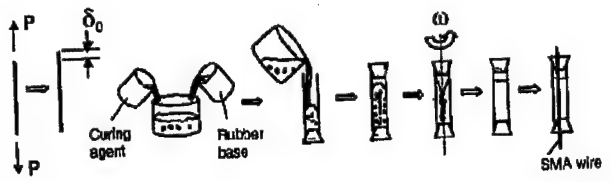

Figure 2: Manufacturing steps of an active SMA composite.

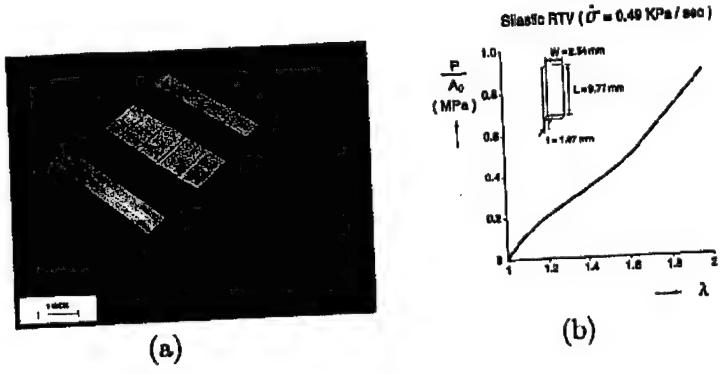

Figure 3: (a) Mold, (b) Stress–stretch response of silicone rubber.

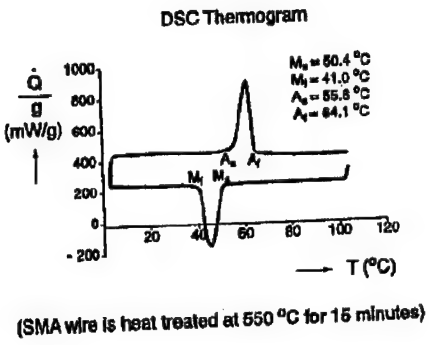

Figure 4: Differential scanning calorimetry of SMA wire.

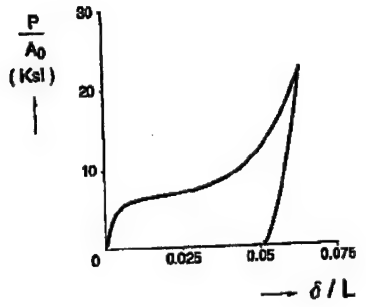

Figure 5: Prestrain cycle of SMA wire.

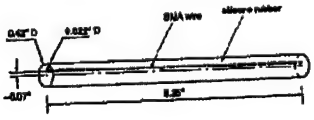

Figure 6: Dimensions of silicone rod with off–axis SMA wire.

Figure 7: Elastomer rod with off–axis SMA wire: (a) 22 °C, (b) 150 °C.

Figure 8: Dimensions (mm) of flat silicone specimen with on–axis SMA wire.

Figure 9: (a) Mold, (b) dogbone specimen with on–axis embedded SMA wires.

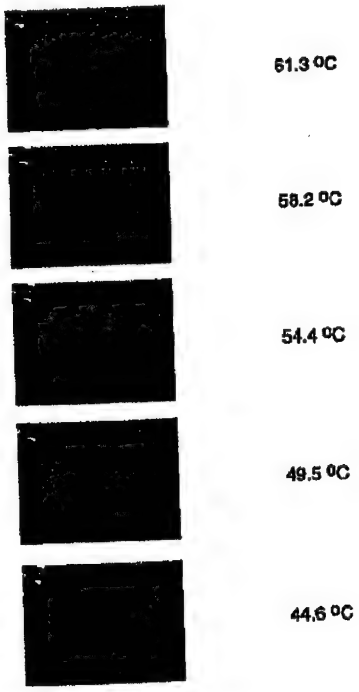

Figure 10: Cantilever beam (cut from gage length of dogbone specimen) self–deflection during cooling.

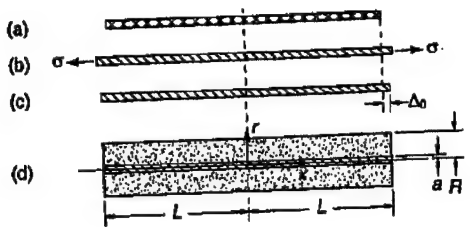

Figure 11: States in the manufacture of a concentric single–fiber SMA active composite: (a) relaxed SMA fiber in twinned martensite state, (b) loaded SMA fiber (detwinned martensite), (c) unloaded prestrained SMA fiber (detwinned martensite), (d) matrix cured in place.

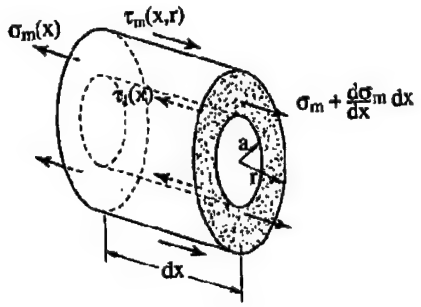

Figure 12: Free body diagram of matrix annulus.

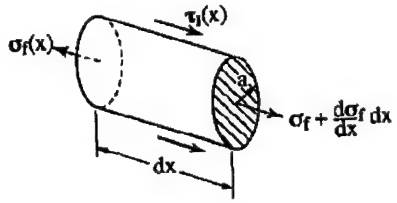

Figure 13: Free body diagram of SMA fiber.

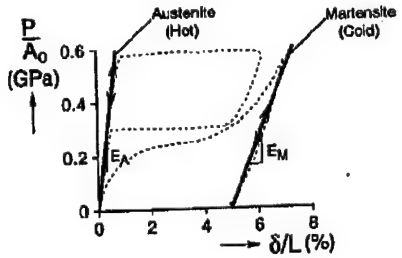

Figure 14: Tensile constitutive response of SMA wire. Bold lines show the idealized elastic response of (a) Hot – austenite, (b) Cold – detwinned martensite.

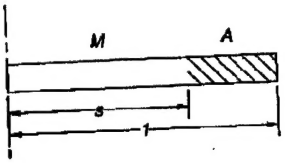

Figure 15: Schematic of partially transformed wire.

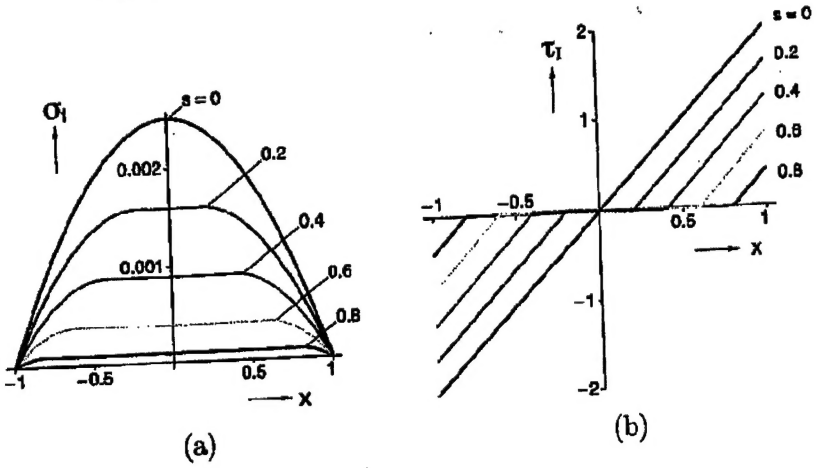

Figure 16: Evolution of non–dimensional stresses with transformation front motion ($a = 0.1185$, $L = 10.46$, $G = 1/70,000$): (a) fiber axial stress, (b) interfacial shear stress.

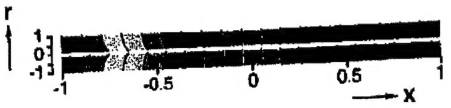

Figure 17: Matrix axial displacement field $u_x(x,r)/L$ after complete transformation to austenite (heating). ($a = 0.1185$, $L = 10.46$, $G = 1/70,000$)

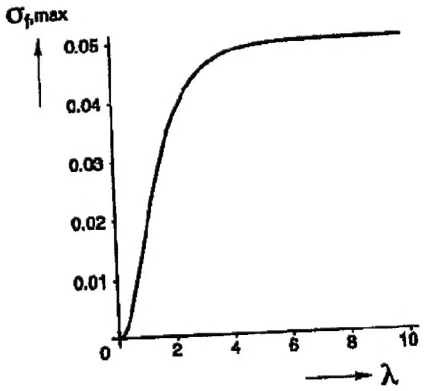

Figure 18: Non–dimensional maximum fiber stress versus Cox parameter λ for $\epsilon_0 = 0.05$.

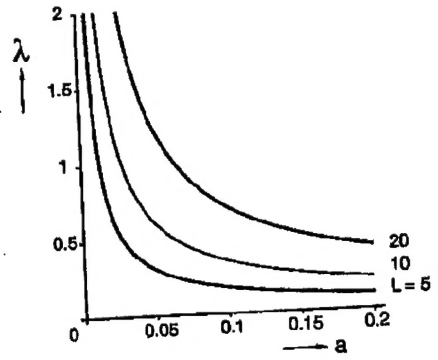

Figure 19: Dependence of λ on geometric parameters for $G = 1/70,000$.

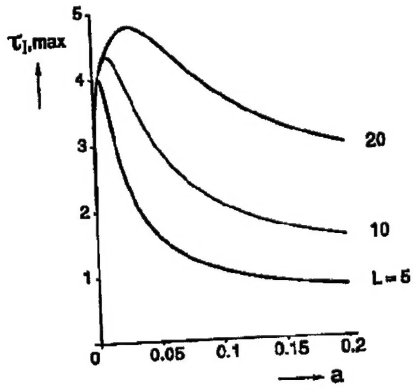

Figure 20: Dependence of non–dimensional maximum interacial shear stress with geometric parameters ($G = 1/70,000$).

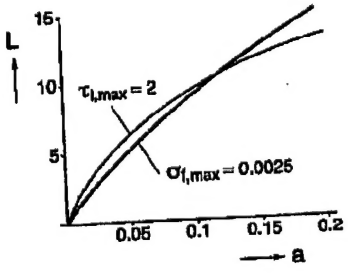

Figure 21: Design curves for maximum fiber stress and interfacial stress for $G = 1/70,000$.

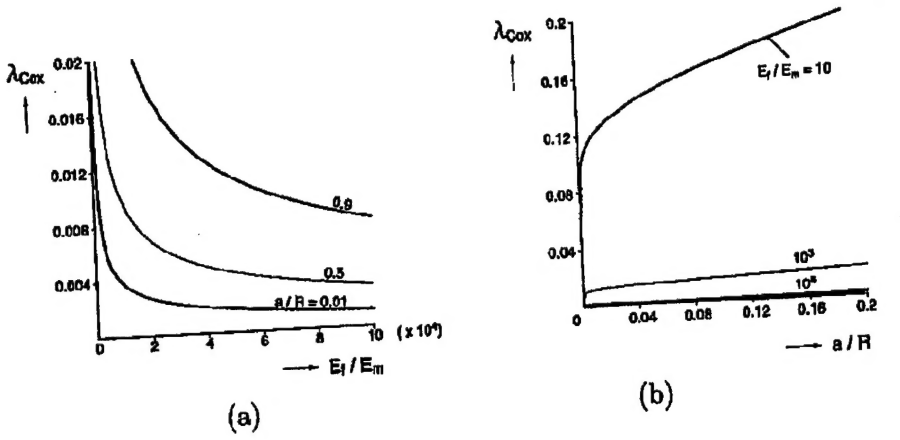

Figure 22: Dependence of Cox λ on geometry and material ratios.

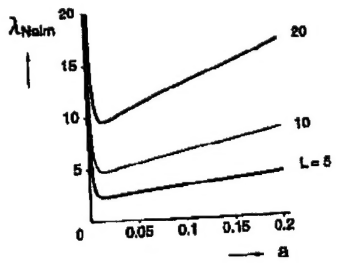

Figure 23: Dependence of Nairn λ on geometry for $E_m = 3/70,000$.

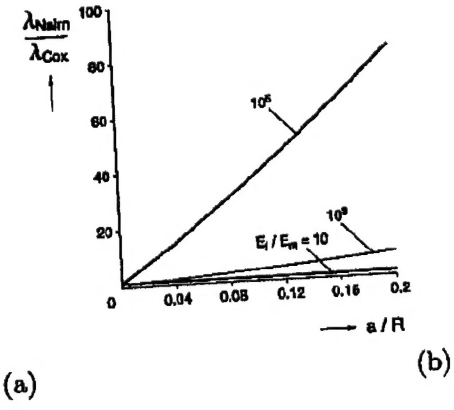

Figure 24: Comparisons of λ between the Cox and Nairn approach.

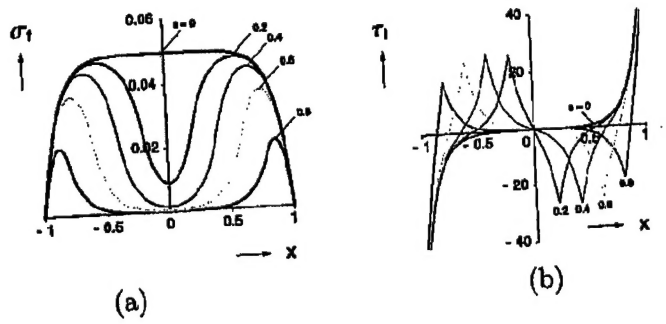

Figure 25: Stress distributions using Nairn λ.